Diamond Mirror for High Power Lasers

H. Atikian[1], P. Latawiec[1], X. Xiong[1,2], S. Meesala[1], S. Gauthier[1], D. Wintz[1], J. Randi[3], D. Bernot[3], S. DeFrances[3], J. Thomas[3], M. Roman[4], S. Durrant[4], F. Capasso[1] and M. Lončar[1]*

Affiliations:

[1] John A. Paulson School of Engineering and Applied Sciences, Harvard University, Cambridge, MA 01238, USA.

[2] Key Laboratory of Quantum Information & Synergetic Innovation Center of Quantum Information & Quantum Physics, University of Science and Technology of China, Hefei, Anhui 230026, China

[3] Penn State University Applied Research Laboratory, Electro-Optics Center, Freeport, PA 16229, USA.

[4] Laser Technology and Analysis Branch, Naval Surface Warfare Center, Dahlgren Division, Dahlgren VA 22448, USA.

*Correspondence to: loncar@seas.harvard.edu

Abstract:

High power lasers are used in a vast number of applications including laser manufacturing (laser cutting and welding), semiconductor industry (advanced photolithography) and medicine (surgical tools). These applications require optical components, mirrors in particular, that can withstand large optical powers in order to transport the optical beams from the laser to the target. Ordinarily, mirrors are implemented as multilayer coatings consisting of thin film dielectric layers of different refractive index and thickness, typically tens to around a hundred layers thick. In high power applications, imperfections and defects in these multi-layers lead to sites where laser energy can be absorbed resulting in significant thermal stress and permanent damage of the component. To address this challenge, we developed monolithic dielectric mirrors that do not suffer from thermally induced damage. Our mirrors are realized by etching nanostructures into a diamond surface, a material that exhibits many favorable optical properties and extremely high thermal conductivity. Our mirrors exhibit reflectivity greater than 98% and operate without sustaining laser induced damage under the irradiation of a 10kW 1070nm laser beam.

One Sentence Summary:

We demonstrate a monolithic all-diamond mirror, implemented by novel surface nanostructuring, capable of withstanding extremely high laser powers.

Main Text:

Modern high-reflectivity dielectric mirrors are based on multi-layered coatings (*1*) or nanostructured thin films (*2*) that allow for precise engineering of the reflection spectrum of transmitted and reflected light. The former utilize alternating thin film layers of varying refractive index and thickness to generate an interference effect at a desired wavelength and polarization, while the latter leverage localized or guided resonances to achieve high reflectivity. Unfortunately, both approaches are not suitable for applications where high power lasers are used. Imperfections and defects created in thin films during deposition or at interfaces between films, form sites where laser energy can be absorbed (*3-5*). At very high laser powers, absorption at these sites generates a tremendous amount of heat causing local melting or extreme thermal stress in the films, degrading the optical performance of the device or resulting in irreversible damage. We overcome this limitation of multi-layered, multi-material optical coatings and demonstrate a monolithic, single-material approach to high-reflectivity mirrors suited for high power laser applications. Our approach is based on diamond substrates, capitalizing on the high thermal conductivity and exceptional optical properties intrinsic to diamond.

Diamond exhibits many favorable material properties for realization of high power optical components including, a relatively high refractive index (2.4), a wide bandgap (5.5eV) and a large optical transmission window ranging from the ultraviolet into the far infrared. Diamond's wide bandgap minimizes the effects of multi-photon absorption, a significant concern at elevated optical powers. Diamond is mechanically hard and chemically resistant, making it suitable for applications in harsh environments. Further, diamond has the highest thermal conductivity of all materials at room temperature (2200W/m•K), and therefore can quickly dissipate any optical energy that may be absorbed (*6-9*).

In this work, we present an all-diamond, high reflectivity mirror etched into the surface of a bulk diamond substrate. The optical properties of the mirror are engineered by nanostructuring of the diamond surface, while simultaneously capitalizing on the high thermal conductivity inherent to bulk diamond. The end result is a robust high reflectivity mirror with exceptional power handling capabilities that are not achievable with traditional multilayered optical coatings.

Diamond mirror design and fabrication

In recent years, photonic crystals and metamaterials have emerged as a promising technology for tailoring properties of optical beams (*10-16*). These are typically composed of two dimensional arrays of holes or rods that allow one to engineer the spatial distribution of amplitude, phase and polarization response of an optical element (*17-22*). Many optical components have been realized using these approaches, such as mirrors, lenses and polarization optics (*23-28*). Conventionally, planar photonic crystals and metamaterials are formed by nanopatterning a high-index dielectric (or metallic) film deposited on a low-index substrate, thus leveraging the index contrast needed to support optical resonances (*29, 30*). Consequently, they are a form of optical coating and thus suffer from the same power handling limitations as their multilayer thin film coating counterparts. By eliminating interfaces between dissimilar materials and fashioning our optic out of a single, pure, crystalline substrate, we entirely avoid the issue of thermally-induced stress for our nanostructured mirror.

Figure 1A illustrates the all-diamond mirror based on a planar array of "golf tee" shaped columns etched directly into a diamond surface. For comparison, Fig. 1B illustrates a traditional multilayered optical coating deposited onto a substrate. By engineering the geometry of each golf

tee column shown in Fig. 1C, namely angle α of the top region, radii r_{disc}, r_{min}, $r_{support}$, total height h and pitch given by the center to center distance between the golf tee columns, it is possible to control the overall reflectivity of the structure as shown in Fig. 1D. High reflectivity of the structure is attributed to a lattice resonance dominated by lateral leaky Bloch modes (*31*). These guided resonances are confined to the top portion of the golf tee column, as seen in Fig.1E, and are not supported by the narrow stems of each column which provides the necessary confinement of the mode. To achieve reflection under normal incidence, parameters of the periodic array must satisfy the well-known grating equation $d(\sin\theta_i - \sin\theta_m) = m\lambda$, where d is the grating period, m is an integer representing the diffraction order, θ_i and θ_m are the angles of the incident beam and angle of the *m*th diffracted order, and λ is the wavelength (*32*). The first diffraction orders are coupled into the resonance supported by the top portion of the column, and then out couple to the zeroth order of the grating in both reflected and transmitted direction. With proper design of parameters for the golf tee structure, incident angle and wavelength, the transmitted beams will interfere destructively resulting in perfect reflection.

Intuitively, this mechanism can be understood in the following way. Each column comprises of three distinct regions of effective refractive index labeled n_1, n_2 and n_3 as highlighted in Fig. 1C. The shaded red area labeled n_2 consists of the top cone feature of the golf tee column. It effectively acts as the high-index layer since it contains more diamond per volume than the other regions. The n_2 region serves as the "guiding layer" for supporting optical resonances in the device. The shaded yellow area labeled n_3 consists of narrow support structures physically holding up the cones in n_2. This is effectively a low-index layer since the supporting structures are significantly thinner than the structures in n_2. The stem is narrow compared to the cone, and will not support an optical mode, thus providing optical confinement in the guiding layer n_2. The shaded yellow area above labeled n_1 is air, providing the condition that effective indices of each region $n_2 > n_1$, n_3 to support optical resonances (*33, 34*).

Simulations using a commercial finite difference time domain (FDTD) solver (Lumerical Inc.), were performed to optimize the structure for reflection at vertical incidence. Figure 1D shows the diamond mirror reflection spectrum for varying design angles α. We design for an operating wavelength of 1064nm, corresponding to the technologically relevant wavelength of 1μm high power lasers. We select the operating point at the dimensions that give the widest bandwidth of high reflectivity. More details on the FDTD simulations along with reflection spectrum for other relevant dimensions are shown in the supplementary materials and Fig. S1-S6.

To realize these complex 3D structures across a wide area sample, we developed an unconventional yet scalable angled etching nanofabrication technique illustrated in Fig.2A. We utilize reactive ion beam angled etching (RIBAE), with oxygen as the reactive gas (*35*). First, an etch mask is patterned onto the substrate surface, Fig.2A (i), followed by a top down etch to the desired vertical depth with the sample mounted perpendicular to the ion beam on a rotating sample mount, Fig.2A (ii). Next, the sample is tilted to obtain an acute angle with respect to the ion beam path. Angled etching is performed at the prescribed angle with the sample stage rotating until the desired undercut has been achieved, Fig.2A (iii). Finally, the etch mask is removed revealing 3D nanostructures etched into the substrate surface, Fig.2A (iv). The key characteristic of this technique is the remarkable uniformity across a wide area potentially as large as 200mm in diameter, only limited by the size of the ion beam source used. Details of RIBAE are discussed in the supplementary materials.

The diamond mirrors are fabricated in type IIa single crystal diamonds grown by chemical vapor deposition (CVD) with less than 5ppb nitrogen concentration. Diamond samples are first cleaned in a boiling mixture of equal parts sulfuric, nitric, and perchloric acid (*36*). A 70nm layer of Nb is deposited onto the surface of the diamond, followed by defining a hydrogen silsesquioxane (HSQ) mask. Top down etch of the Nb and diamond is performed, etching circular pillars onto the surface, with subsequent removal of the HSQ mask using hydrofluoric acid (HF). RIBAE is performed at a 70º angle until the desired etch depth is achieved, followed by the removal of the Nb mask. Complete fabrication details are given in the supplementary materials. Figure 2B shows an optical image of the diamond mirror, with a ruler in the frame as a reference. Figure 2C shows a scanning electron microscope (SEM) image of the fabricated diamond mirror, clearly showing the golf tee columns forming the diamond mirror. Figure 2D shows a zoomed in SEM image of the golf tee features. The overall patterned area of the diamond mirror is 3mm x 3mm, with nearly identical device geometry from one edge of the substrate to the other. The ability to precisely and uniformly fabricate nanometer scale geometries across a large surface was enabled by the RIBAE technique.

Diamond mirror characterization

The diamond mirror absolute reflectivity and reflection spectrum are measured using the experimental setup shown in Fig S8. Details on the measurement setup and experimental procedures are given in the supplementary materials. Figure 3A shows the reflection spectrum from the diamond mirror, showing excellent agreement with theoretical predictions. Since the patterned area of the mirror is only 3mm x 3mm, a collimated superluminescent diode with peak wavelength λ=1065nm was used to focus a spot of less than 1mm on the nanostructured surface and an optical spectrum analyzer was used to capture the reflection spectrum. Absolute reflectivity at λ=1064nm was measured to be 98.9 +/- 0.5% using a 1064nm Distributed Bragg reflector (DBR) laser with a 10MHz linewidth and a free space optical power detector, and around 0.5% of the power transmitted through the diamond substrate with a polished backside surface. Greater than 98% reflectivity is observed across a 10nm bandwidth around the operating wavelength. Beam profile measurements using a scanning slit profiler are performed on the reflected beam from the diamond mirror to ensure the incident Gaussian beam is not distorted. Figure 3B illustrates a 2D intensity plot of a reflected beam from the diamond mirror with a 4σ beam width of ~1.5mm. The X and Y axis show cross section profiles of the reflected beam with an overlaid Gaussian fit. The inset in Fig. 3B shows a 3D perspective of the reflected beam, further illustrating how the nanostructured diamond mirror does not distort the incident Gaussian beam profile. Figure S6 in the supplementary materials provides FDTD simulations of the reflection phase from the diamond mirror, further showing how the nanostructured diamond surface maintains a uniform phase-front for reflected beams.

Laser damage testing

Laser induced damage threshold (LIDT) of the diamond mirror was assessed using a λ=1070 nm multimode fiber laser from IPG Photonics, capable of providing up to 10 kW of continuous wave (CW) laser power. The test laser was focused down to a spot of 750µm ($1/e^2$) diameter and centered on the 3mm x 3mm mirror (patterned) area. This ensures that the optical beam spans hundreds of periods in the diamond mirror lattice. A diamond mirror designed for a central spectral position of λ=1070nm, aligned to the center wavelength of the IPG laser, was mounted on an aluminum water cooled mount during laser damage testing. Figure S9 provides the measured and simulated reflection spectrum of the diamond mirror, along with an overlay of the

10kW IPG laser spectrum in arbitrary units. Figure S10 illustrates the beam profile of the IPG test laser, along with the Gaussian fit. Further details of the LIDT testing setup and procedure are provided in the supplementary materials.

The sample was optically monitored with an off-axis camera for in-situ inspection and digital image capture of the irradiated surface. A FLIR thermal imaging camera was also used to monitor the temperature of the apparatus throughout testing. Damage testing was performed at approximately 2-3° off normal incidence to avoid the reflected beam returning into the laser. The laser intensity was incrementally increased from 500W to 10kW. At each power level, the diamond mirror was irradiated for 60 seconds. Figure 4 summarizes the results on the LIDT testing. Fig. 4A shows an optical image of the diamond mirror mounted on the water cooled sample mount. Fig 4.(B-E) shows the thermal image capture of the mounted diamond mirror at varying power levels of 500W, 2.5kW, 5kW and 10kW, respectively. The hot spot in the image indicates the area of interest being irradiated with the high power laser. A small fraction of the laser power leaks through the diamond mirror and is absorbed by the aluminum water cooled mount supporting the diamond. This can be seen in Fig. S9, where the spectrum of the IPG laser is not perfectly aligned with the maximum reflectivity of the mirror allowing about 4% of the laser energy to transmit through the diamond. The temperature increase captured by the thermal camera is attributed to the local heating of the sample mount due to the transmitted power. We provide video demonstration for the LIDT tests in the supplementary materials, of the thermal imaging video capture for power levels 500W, 2.5kW, 5kW, 7.5kW and 10kW, in movies S1-S5, respectively. Movie S6, provides video capture of a test performed at 10kW, illustrating the power leaking through the diamond and being absorbed by the water cooled mount. At this maximum intensity level, the diamond mirror maintained its reflectivity, and had no indication of damage or change in surface morphology by optical or SEM inspection, proving to be far superior to existing high power mirrors and optics (*37-39*).

Conclusions and Outlook

In this work, we demonstrated a monolithic diamond mirror fabricated from a bulk diamond substrate, creating an optical component that behaves as a highly reflective surface, while still retaining the extraordinary material properties diamond has to offer. This is confirmed by beam profile measurements and numerical modeling, where no distortions in the reflected laser beam has been observed. Laser damage testing demonstrated the exceptional ability of the all-diamond mirror to operate under high power laser illumination. We believe that our work will stimulate development of a new class of optical components for high power laser applications across the optical spectrum. Applications in directed energy, or extreme ultraviolet (EUV) lithography systems that utilize high power CO_2 lasers, will benefit from a new category of monolithic optics capable of operating in extreme conditions (*40*). Finally, it is important to note that this technology is not limited to diamond alone. Using the same technique one can fabricate reflectors from a wide variety of bulk substrates. For example, monolithic mirrors made from fused silica could be very interesting in ultrafast pulsed laser applications, where the damage mechanism is dominated by dielectric breakdown. The extremely large bandgap (~9eV) fused silica provides, along with the monolithic nature of these mirrors could show significant improvement in ultrafast applications.

References:

1. P. W. Baumeister, Optical coating technology. *Optimization* **10**, 7 (2004).
2. S. Fan, J. D. Joannopoulos, Analysis of guided resonances in photonic crystal slabs. *Physical Review B* **65**, 235112 (2002).
3. L. N. Taylor, A. K. Brown, A. J. Pung, E. G. Johnson, J. J. Talghader, Continuous-wave laser damage of uniform and nanolaminate hafnia and titania optical coatings. *Opt. Lett.* **38**, 4292-4295 (2013).
4. D. Ristau, *Laser-Induced Damage in Optical Materials*. (CRC Press, 2014).
5. D. Ristau, M. Jupé, K. Starke, Laser damage thresholds of optical coatings. *Thin Solid Films* **518**, 1607-1613 (2009).
6. G. Davies, *Properties and Growth of Diamond*. (Inspec, 1994).
7. M. Karlsson, F. Nikolajeff, Diamond micro-optics: microlenses and antireflection structured surfaces for the infrared spectral region. *Opt. Express* **11**, 502-507 (2003).
8. C. J. Brierley, C. M. Beck, G. R. Kennedy, J. Metcalfe, D. Wheatley, The potential of CVD diamond as a replacement to ZnSe in CO2 laser optics. *Diamond and Related Materials* **8**, 1759-1764 (1999).
9. A. M. Zaitsev, *Optical Properties of Diamond A Data Handbook*. (Springer, 2001).
10. W. Cai, V. Shalaev, *Optical Metamaterials: Fundamentals and Applications*. (Springer, 2009).
11. N. Engheta, R. W. Ziolkowski, *Metamaterials: Physics and Engineering Explorations*. (Wiley-IEEE 2006).
12. J. B. Pendry, D. Schurig, D. R. Smith, Controlling Electromagnetic Fields. *Science* **312**, 1780 (2006).
13. P. Qiao, W. Yang, C. J. Chang-Hasnain, Recent advances in high-contrast metastructures, metasurfaces, and photonic crystals. *Adv. Opt. Photon.* **10**, 180-245 (2018).
14. I. Staude *et al.*, Tailoring Directional Scattering through Magnetic and Electric Resonances in Subwavelength Silicon Nanodisks. *ACS Nano* **7**, 7824-7832 (2013).
15. N. Yu, F. Capasso, Flat optics with designer metasurfaces. *Nat Mater* **13**, 139-150 (2014).
16. N. Yu *et al.*, Light Propagation with Phase Discontinuities: Generalized Laws of Reflection and Refraction. *Science* **334**, 333 (2011).
17. F. Aieta, M. A. Kats, P. Genevet, F. Capasso, Multiwavelength achromatic metasurfaces by dispersive phase compensation. *Science* **347**, 1342 (2015).
18. M. Esfandyarpour, E. C. Garnett, Y. Cui, M. D. McGehee, M. L. Brongersma, Metamaterial mirrors in optoelectronic devices. *Nat Nano* **9**, 542-547 (2014).
19. A. V. Kildishev, A. Boltasseva, V. M. Shalaev, Planar Photonics with Metasurfaces. *Science* **339**, (2013).
20. Y. Yang, I. I. Kravchenko, D. P. Briggs, J. Valentine, All-dielectric metasurface analogue of electromagnetically induced transparency. *Nature Communications* **5**, 5753 (2014).
21. Y. H. Fu, A. I. Kuznetsov, A. E. Miroshnichenko, Y. F. Yu, B. Luk'yanchuk, Directional visible light scattering by silicon nanoparticles. *Nature Communications* **4**, 1527 (2013).
22. A. Arbabi, Y. Horie, M. Bagheri, A. Faraon, Dielectric metasurfaces for complete control of phase and polarization with subwavelength spatial resolution and high transmission. *Nature Nanotechnology* **10**, 937 (2015).
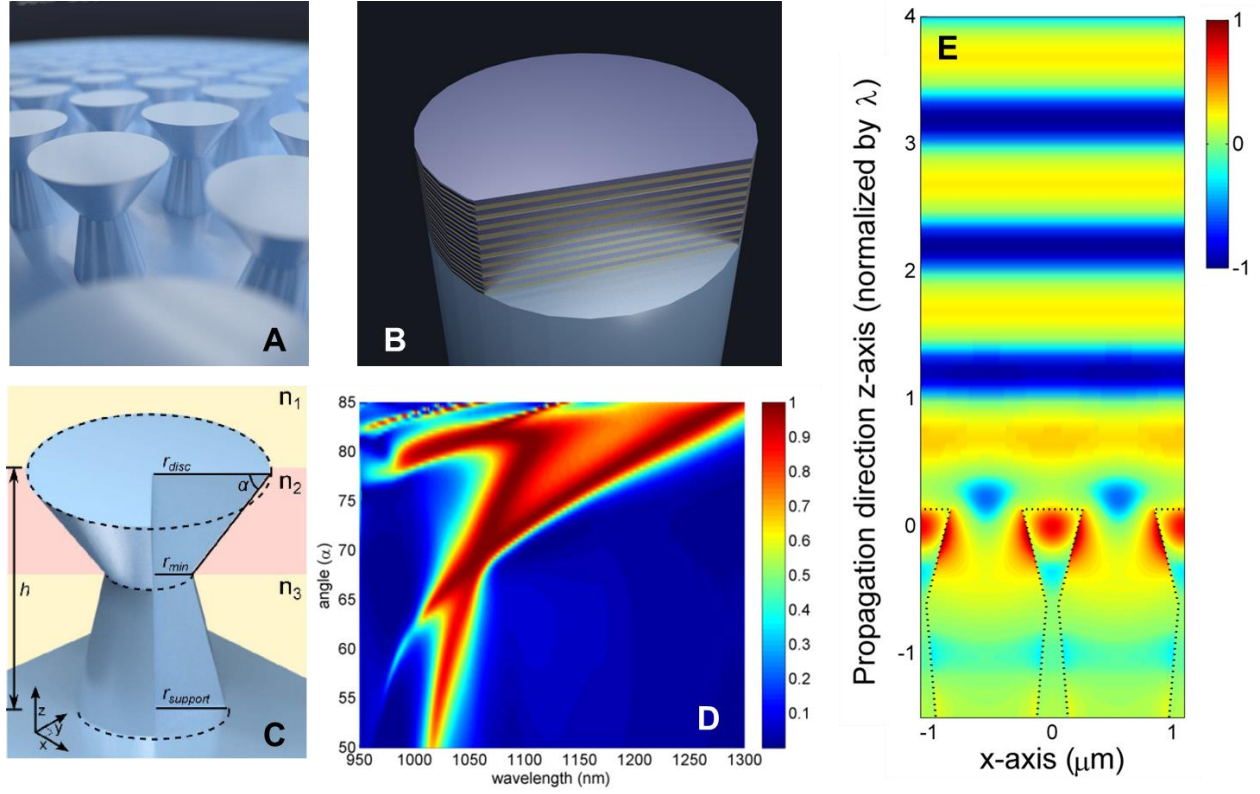
23. M. Khorasaninejad, F. Capasso, Metalenses: Versatile multifunctional photonic components. *Science* **358**, eaam8100 (2017).
24. M. Khorasaninejad *et al.*, Metalenses at visible wavelengths: Diffraction-limited focusing and subwavelength resolution imaging. *Science* **352**, 1190 (2016).
25. S. Liu *et al.*, Optical magnetic mirrors without metals. *Optica* **1**, 250-256 (2014).
26. P. Moitra, B. A. Slovick, Z. Gang Yu, S. Krishnamurthy, J. Valentine, Experimental demonstration of a broadband all-dielectric metamaterial perfect reflector. *Applied Physics Letters* **104**, 171102 (2014).
27. P. Moitra *et al.*, Large-Scale All-Dielectric Metamaterial Perfect Reflectors. *ACS Photonics* **2**, 692-698 (2015).
28. B. Slovick, Z. G. Yu, M. Berding, S. Krishnamurthy, Perfect dielectric-metamaterial reflector. *Physical Review B* **88**, 165116 (2013).
29. J. D. Joannopoulos, S. G. Johnson, J. N. Winn, R. D. Meade, *Photonic Crystals: Molding the Flow of Light, 2nd ed.* (Princeton University Press, 2008).
30. S. S. Wang, R. Magnusson, Theory and applications of guided-mode resonance filters. *Appl. Opt.* **32**, 2606-2613 (1993).
31. Y. H. Ko, R. Magnusson, Wideband dielectric metamaterial reflectors: Mie scattering or leaky Bloch mode resonance? *Optica* **5**, 289-294 (2018).
32. D. Rosenblatt, A. Sharon, A. A. Friesem, Resonant grating waveguide structures. *IEEE Journal of Quantum Electronics* **33**, 2038-2059 (1997).
33. S. Tibuleac, R. Magnusson, Reflection and transmission guided-mode resonance filters. *J. Opt. Soc. Am. A* **14**, 1617-1626 (1997).
34. H. L. Bertoni, L. h. S. Cheo, T. Tamir, Frequency-selective reflection and transmission by a periodic dielectric layer. *IEEE Transactions on Antennas and Propagation* **37**, 78-83 (1989).
35. H. A. Atikian *et al.*, Freestanding nanostructures via reactive ion beam angled etching. *APL Photonics* **2**, 051301 (2017).
36. H. A. Atikian *et al.*, Superconducting nanowire single photon detector on diamond. *Applied Physics Letters* **104**, 122602 (2014).
37. E. Anoikin, A. Muhr, A. Bennett, D. Twitchen, H. de Wit. (2015), vol. 9346, pp. 93460T-93460T-93469.
38. L. S. Meng, J. K. Brasseur, D. K. Neumann, Damage threshold and surface distortion measurement for high-reflectance, low-loss mirrors to 100+ MW/cm2 cw laser intensity. *Opt. Express* **13**, 10085-10091 (2005).
39. C. S. Menoni *et al.*, in *Optical Interference Coatings 2016*. (Optical Society of America, Tucson, Arizona, 2016), pp. ThA.10.
40. D. C. Brandt *et al.*, in *Emerging Lithographic Technologies XI*. (International Society for Optics and Photonics, 2007), vol. 6517, pp. 65170Q.

Acknowledgments:

Fig. 1 Diamond mirror design and simulation. (**A**) Graphical depiction of the diamond mirror with the golf tee columns placed in a hexagonal lattice. (**B**) Typical multilayered optical coating deposited onto a substrate. (**C**) Schematic of the golf tee column constituting the diamond mirror, with all relevant dimensions labeled: angle α, radii r_{disc}, r_{min}, $r_{support}$, and total height h. Shaded yellow area labeled n_1 is a low index region, in this case air. Shaded red area n_2 is the top portion of the golf tee column which supports the optical resonances. Shaded yellow area n_3 is a low index region containing the lower portion of the golf tee column, serving as a physical support to hold up the optical structure in n_2. (**D**) Diamond mirror reflection spectrum at normal incidence for varying design angles α, with r_{disc} =250nm, r_{min} =50nm, $r_{support}$ =250nm, pitch 1.1μm, and height 3μm. Red and blue colors indicate locations of maximum and minimum reflection respectively. (**E**) Standing-wave pattern illustrating the reflected wavefront from the diamond mirror at the 1064nm. Mode is confined in the top portion of the golf tee structure.
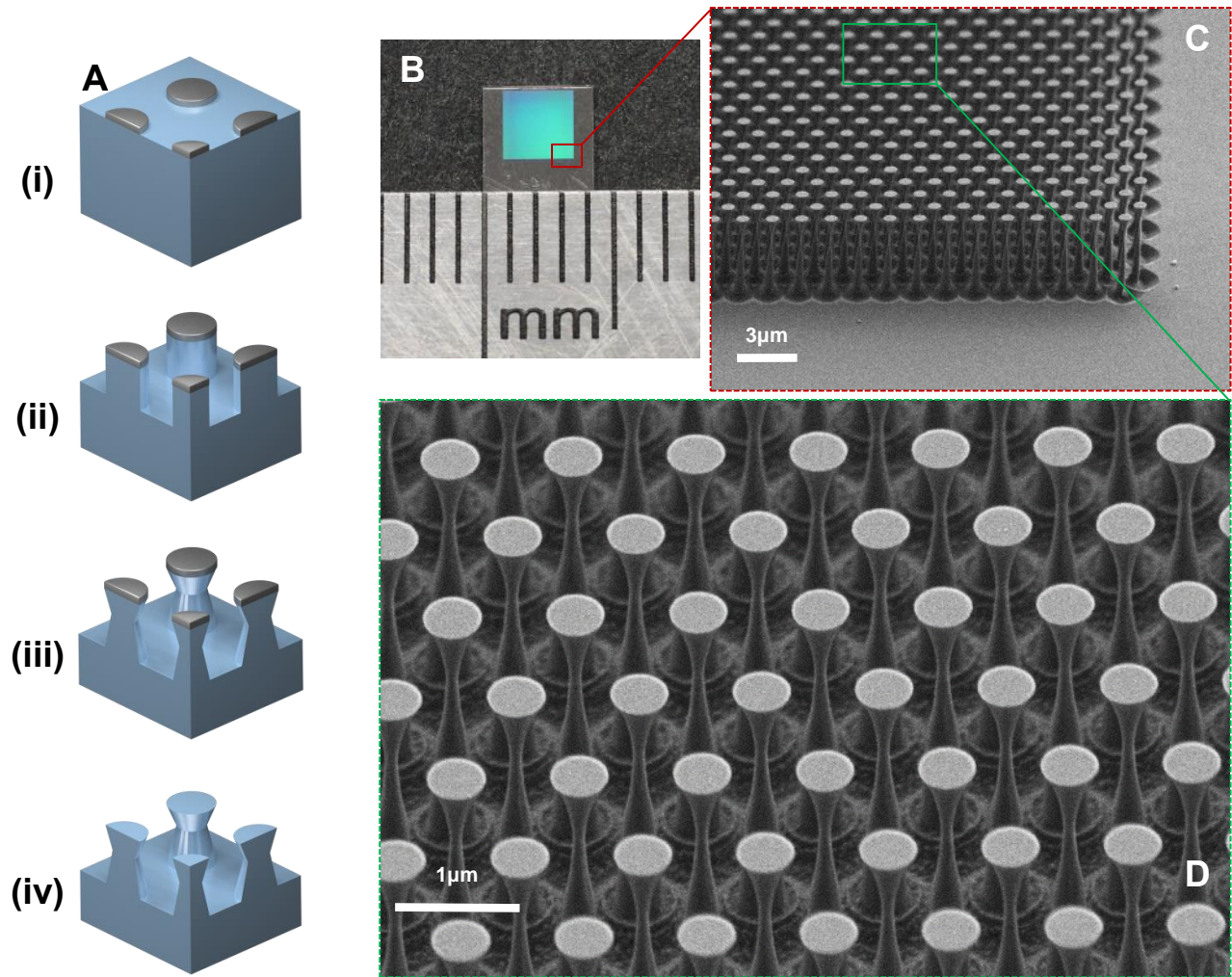
Fig. 2 Diamond mirror fabrication and device images. **(A)** Schematic of reactive ion beam angled etching (RIBAE) fabrication process. (i) Etch mask is patterned onto the substrate surface. (ii) Top-down etch with the sample mounted perpendicular to the ion beam path on a rotating sample stage. (iii) Sample tilted during etching to obtain an acute angle between the sample and ion beam, uniformly etching underneath the etch mask. (iv) Mask removal yielding freestanding nanostructures from a bulk substrate. **(B)** Optical image of the diamond mirror on a 4.2mm x 4.2mm diamond. Each division on the ruler is 1mm. **(C)** SEM image of the diamond mirror taken at 60º. **(D)** Zoomed in SEM image of golf tee features for the diamond mirror taken at 40º.
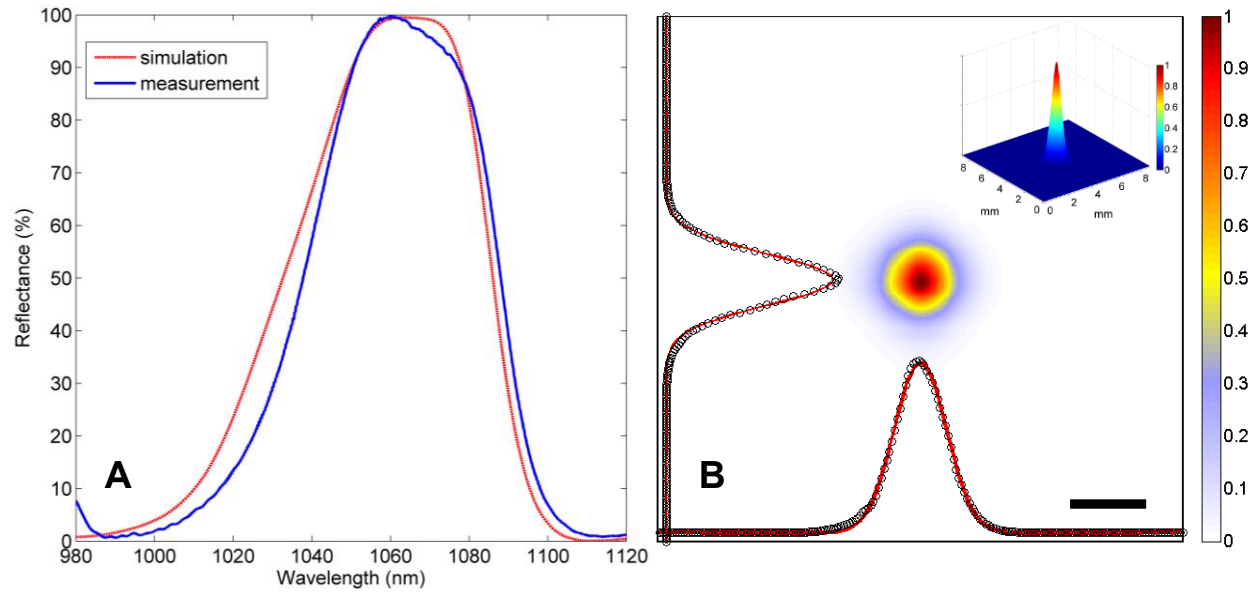
Fig. 3 Optical characterization of the diamond mirror. **(A)** Reflection spectrum of the diamond mirror, blue line is measurement data and red line is FDTD simulation. Superluminescent diode center at λ=1060nm and a Yokogawa optical spectrum analyzer used to capture the spectrum. Absolute reflectivity of 98.9 +/- 0.5% measured at 1064nm using a DBR laser with a 10MHz linewidth **(B)** Beam profile measurement taken of the reflected beam from the diamond mirror using a scanning slit profiler. X-Y axis show cross sections of the reflected beam (black circles) with overlaid Gaussian fit (red). 1mm scale bar. Inset shows a 3D perspective of the reflected beam.
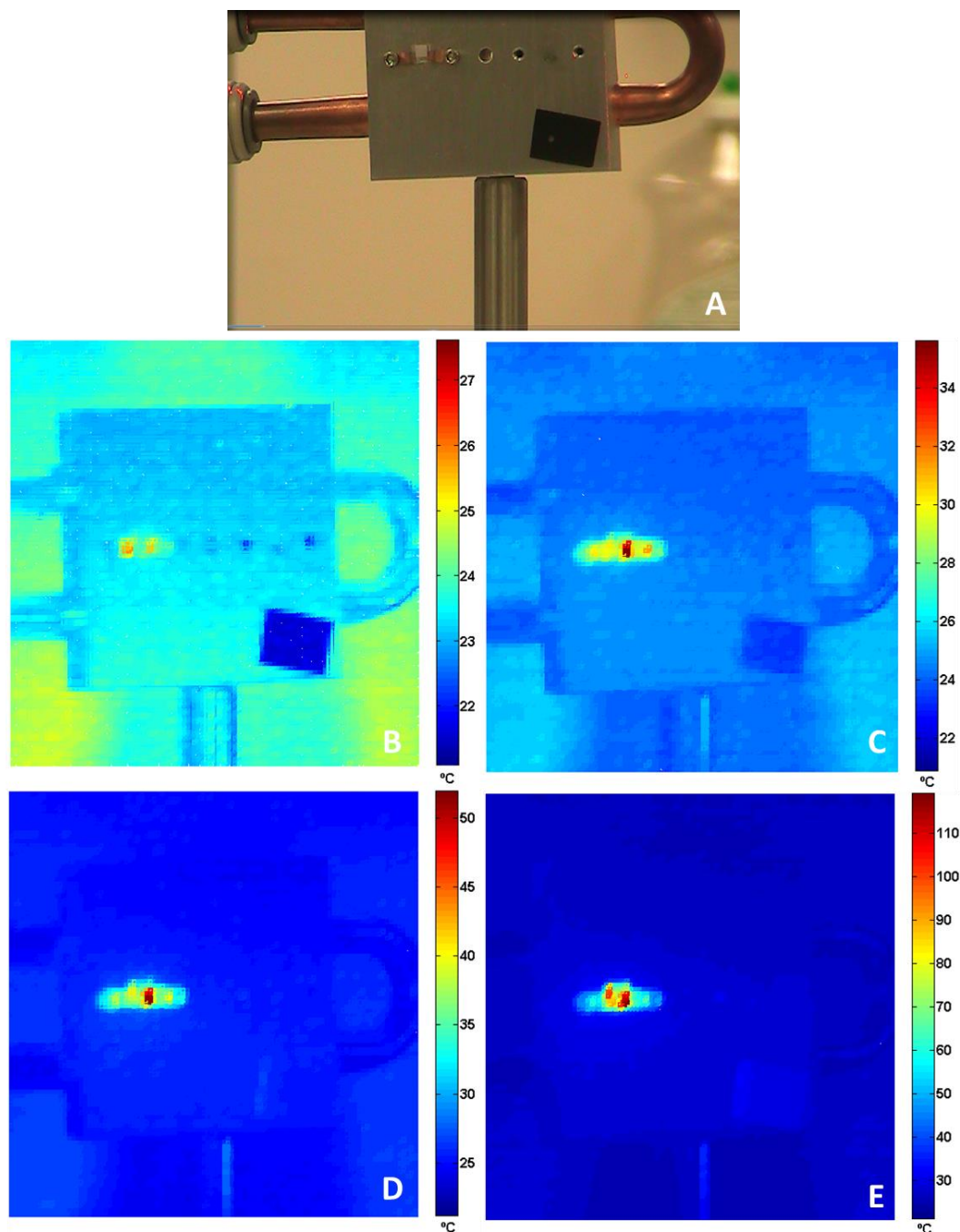
Fig. 4 Laser induced damage threshold (LIDT) of the diamond mirror. (A) Optical image of the diamond mirror mounted on the water cooled sample mount. (B-E) thermal image of diamond mirror at 500W, 2.5kW, 5kW and 10kW irradiance by an IPG multimode fiber laser. Color bar shows the temperature of the diamond mirror mounted on a water cooled aluminum mount, at increased power levels the small fraction of optical power leaking through the backside of the diamond mirror results in heating of the aluminum sample stage. Hot spot in the image corresponds to the center position of the diamond mirror irradiated by the high power laser, coincident with the location of temperature increase.

Supplementary Materials:

Materials and Methods

Figures S1-S10

Movies S1-S6

Supplementary Materials for

Diamond Mirror for High Power Lasers

H. Atikian[1], P. Latawiec[1], X. Xiong[1], S. Meesala[1], S. Gauthier[1], D. Wintz[1], J. Randi[2], D. Bernot[2], S. DeFrances[2], J. Thomas[2], M. Roman[3], S. Durrant[3], F. Capasso[1] and M. Lončar[1]*

Correspondence to: loncar@seas.harvard.edu

This PDF file includes:

> Materials and Methods
> Figs. S1 to S10
> Captions for Movies S1 to S6

Other Supplementary Materials for this manuscript include the following:

> Movies S1 to S6

Materials and Methods

FDTD design and simulations

Simulations were performed using a commercial finite difference time domain (FDTD) solver (Lumerical Inc.). In all simulations, periodic boundary conditions were applied in the x and y directions with a plane wave source as the input to the structure. Schematic of the golf tee columns constituting the diamond mirror is shown in Fig. 1C with all relevant dimensions labeled. Figure S1 shows the reflection spectrum for the diamond mirror for varying radius r_{disc}, showing the wide spectrally tunable range of the design. It is important to note that the radius of the cone is directly controlled by the precision of the electron beam lithography tool, where nanometer accuracy is attainable. Figure S2 plots the reflection spectrum for varying radius r_{min}, this dimension is the neck of the golf tee column defining the minimum radius of the pinch-point. When $r_{min} < 75$nm both the maximum reflection and the spectral position of the maximum reflection are unchanged, belying the device's robustness in fabrication. At a radius greater than 75nm, the optical mode begins to leak into the support structure and into the substrate abruptly reducing the reflectivity of the diamond mirror. Figure S3 plots the reflection spectrum for varying radius $r_{support}$, this is the radius of the supporting structure at the bottom of the golf tee column. When $r_{support} < 300$nm the magnitude and spectral position of maximum reflection are again maintained. Figure S4 plots the reflection spectrum for varying overall device height *h*. When *h* > 3µm the maximum bandwidth for high reflection is maintained. Again, the total height does not affect the spectral position of the mirror, resulting in a design which is very robust to fabrication tolerances. Figure S5 plots the reflection spectrum for varying pitch of the diamond mirror. Pitch is defined as the center to center distance of the golf tee columns in a hexagonal lattice. We observe that by varying pitch; a wide spectral tuning range can be achieved.

Further FDTD modeling is done to probe into the resonant nature of the diamond mirror. Figure S6A shows a sectional line-cut of the golf tee design angle at α = 75º, indicated by the dashed white line. The reflectance of this line is extracted in Fig. S6B clearly indicating the existence of two resonance modes at the reflection maxima. The two peaks correspond to the electric and magnetic dipole resonances, with the insets illustrating the electric field and magnetic field profiles in the x-y plane at z = 0µm. Figure S6C illustrates the electric and magnetic field vector plots for their respective resonances. The E and H fields are perpendicular to each other, further confirming the existence of clear electric and magnetic dipole resonances in the golf tee structure. FDTD modeling is done to generate maps of the standing-wave patterns reflected from the diamond mirror. Figures S6D and S6E illustrate the reflected electric fields at both the electric and magnetic resonance wavelengths of the diamond mirror and compares them to the field maps obtained from a perfect electric conductor (PEC) mirror (25). Figure S6D shows the standing wave patterns for the diamond mirror and the PEC mirror at the electric dipole resonance wavelength. The reflection phase at this wavelength is close to 180º, consistent with the reflection phase obtained from a PEC where the electric field component at the PEC-air boundary is always pinned to zero. Figure S6E illustrates the standing-wave patterns for the diamond mirror and PEC mirror at the magnetic dipole resonance wavelength. The reflection phase at this wavelength remains close to zero, consistent with a magnetic mirror. In both plots the standing wave patterns are normalized to their respective electric or magnetic dipole

resonance wavelengths, clearly demonstrating the respective phase shift in the standing-wave patterns generated by the diamond mirror at both resonance positions.

Device fabrication

To realize these complex 3D structures across a wide area sample, we developed an unconventional, yet novel and scalable angled etching nanofabrication technique, utilizing an etching process called reactive ion beam etching (RIBE). RIBE is a derivative of ion beam etching (IBE) where a broad area ion beam source is used to collimate and direct a beam of high energy ions from a gas source. The distinction for RIBE is that the plasma source is compatible with reactive gases, whereas IBE is limited to noble gases such as Ar, Xe, or Ne. In our cases we use O_2 as a reactive gas to etch diamond. Ions are extracted from the plasma source using a set of electrically biased grids, typically made from molybdenum. Voltages applied to these grids, along with the plasma source, dictate the ion energy, ion flux and ion divergence exiting the ion source through the grids. Typically the uniformity of the ion beam across the diameter of the ion source can be less than 5%, with the physical diameter of the ion source being the only limitation on the wafer size that can be processed.

Figure S7 depicts the fabrication procedure used to create the diamond mirror from now on referred to as reactive ion beam angled etching (RIBAE) (35). First an etch mask is patterned onto the sample surface. This is followed by a top down etch with the sample mounted perpendicular to the ion beam path on a rotating sample stage, Fig. S7B(i). Once the desired vertical depth has been reached the sample is tilted to an acute angle with the ion beam path. The sample remains rotating on the sample stage, uniformly undercutting the sample in all directions as seen in Fig. S7B(ii). Finally the etch mask is removed revealing the undercut structures etched into the bulk diamond substrate, Fig. S7B(iii).

We utilize the RIBAE technique to etch the golf tee column nanostructures across a wide area on diamond substrates to form the mirror. The diamond mirrors are fabricated in type IIa single crystal diamonds (Element 6) grown by CVD with less than 5ppb nitrogen concentration. Diamond samples are first cleaned in a boiling mixture of equal parts sulfuric, nitric, and perchloric acid (36). A 70nm layer of Nb is deposited onto the surface of the diamond by DC magnetron sputtering, followed by spin coating with hydrogen silsesquioxane (HSQ) resist, patterning via 125keV electron beam lithography and developed in a 25% tetramethylammonium hydroxide solution. Top down etch of the Nb film is performed in a UNAXIS Shuttleline inductively coupled plasma reactive ion etcher (ICP-RIE), with the following parameters: 400W ICP power, 250W radio frequency (RF) power, 40sccm Ar flow rate, 25sccm Cl_2 flow rate and 8mTorr process pressure.

The rest of the fabrication flow follows the RIBAE process using a Kaufman & Robinson 14cm diamond RF-ICP ion beam source. RIBAE parameters are as follows: beam voltage 200V, accelerator voltage 26V, beam current 85mA, ICP power ~155W, O_2 flow 37sccm, and process pressure 7.5×10^{-4} Torr. A non-immersed electron source neutralizer is used to neutralize the positive ions in the ion beam. The neutralizer is mounted on the side of the ion source with the emission current set to x1.25 the ion source beam current and Ar gas flow of 10sccm. The first step is the top down etch of the diamond to achieve the desired vertical depth of the structures.

This is followed by removal of the HSQ mask via hydrofluoric acid (HF). Nb does not react with HF, leaving the Nb mask intact to serve as the etch mask during the angled etching process. The reasoning for the 70nm Nb mask is two-fold. First, it is an excellent etch mask for oxygen plasma, providing ample selectivity to create the desired structures without significant mask erosion. Second, a thin mask is required such that when the sample is tilted to an acute angle, the height of the resist should not shadow neighboring nanostructures. This restriction puts an ultimate limit to how close patterns can be relative to each other and still create undercut structures. RIBAE is performed at a 70º angle until the desired undercut is achieved. This is followed by the removal of the Nb mask using buffered chemical polish (BCP). BCP consists of 2 parts 85% phosphoric acid to 1 part 49% hydrofluoric acid to 1 part 70% nitric acid. The sample is then rinsed in deionized water, followed by a solvent clean with acetone and isopropyl alcohol.

Experimental setup for reflectance measurements and beam profile

The reflection spectrum and absolute reflectivity of the diamond mirror was measured using the setup seen in Fig. S8. For spectral measurements a 1065nm superluminescence diode (InPhenix IPSDD1004C) is collimated and directed with broadband silver mirrors (Thorlabs PF10-03-P01). A 50:50 beamspiltter (Thorlabs CM1-BP145B3) is used to direct the reflected beam to an optical spectrum analyzer (Yokogawa AQ6370). Lenses are used to focus the beam to the sample (Thorlabs AC254-300-C-ML). Because the patterned sample area is limited to (3mm x3mm) we use a long focal length lens (f=300mm) to adjust the size of the beam at the diamond mirror to be less than 1mm. A reference spectrum is taken with a broadband silver mirror at the device under test (DUT) location. Next, the diamond mirror is placed in the setup and the device spectrum is obtained by normalizing with the reference.

For absolute reflectivity measurements, the laser source is replaced by a 1064nm DBR laser with a 10MHz linewidth (Thorlabs DBR1064S) and detected with a free space optical photodetector (Newport 918D-SL-OD3R). A reference power measurement is taken with a Nd:YAG laser line mirror with R>99.5% (Thorlabs NB1-K14). This value is normalized to the power reading taken with the diamond mirror to get absolute reflectivity at 1064nm.

Beam profile measurements were performed using the 1064nm DBR laser with a scanning slit beam profiler (Thorlabs BP209-IR), in place of the detector in Fig. S8. A least squares method was used to fit the X-Y cross section profile of the beam in Fig. 3B.

Experimental setup for laser damage testing

Laser induced damage threshold (LIDT) of the diamond mirror was assessed at Penn State University Applied Research Laboratory, Electro-Optics Center. The laser source used for testing is a 1070 nm multimode fiber laser from IPG Photonics, capable of providing up to 10 kW of continuous wave (CW) laser power. A diamond mirror designed for a central spectral position of $\lambda = 1070$nm, aligned to the center wavelength of the IPG laser, was mounted on an aluminum water cooled mount (Aavid 416401U00000G). Figure S9 provides the measured and simulated reflection spectrum of the diamond mirror, along with an overlay of the 10kW IPG laser spectrum in arbitrary units. The water cooled mount was connected to a chiller set to 18°C

with a flow of approximately 7.5 liters per minute. A 500mm lens focused the laser down at the sample to a spot of 750µm ($1/e^2$) diameter. The beam profile is collected at high laser powers using a Primes focus monitor, beam profile and Gaussian fit are shown in Fig. S10. The focus monitor has a metal tip with a 20um pinhole in the side. The rotating tip then traverses the entire area of the beam, collecting 2D data of the beam profile. The system has a motorized Z-axis to move the measurement plane to the exact desired location.
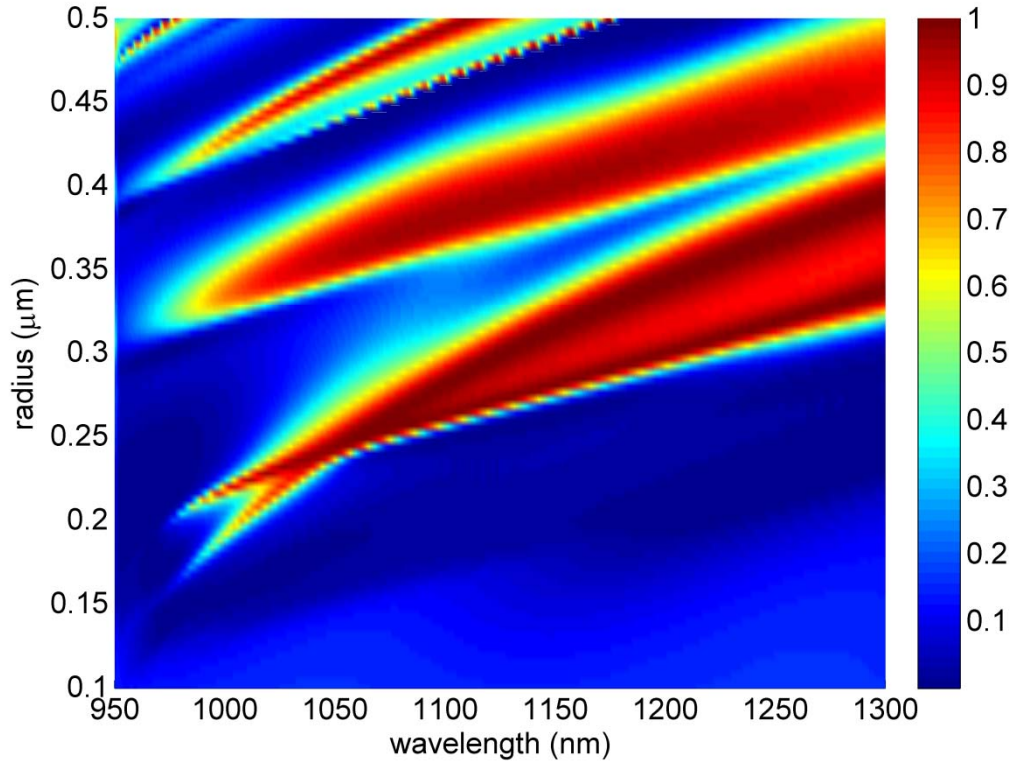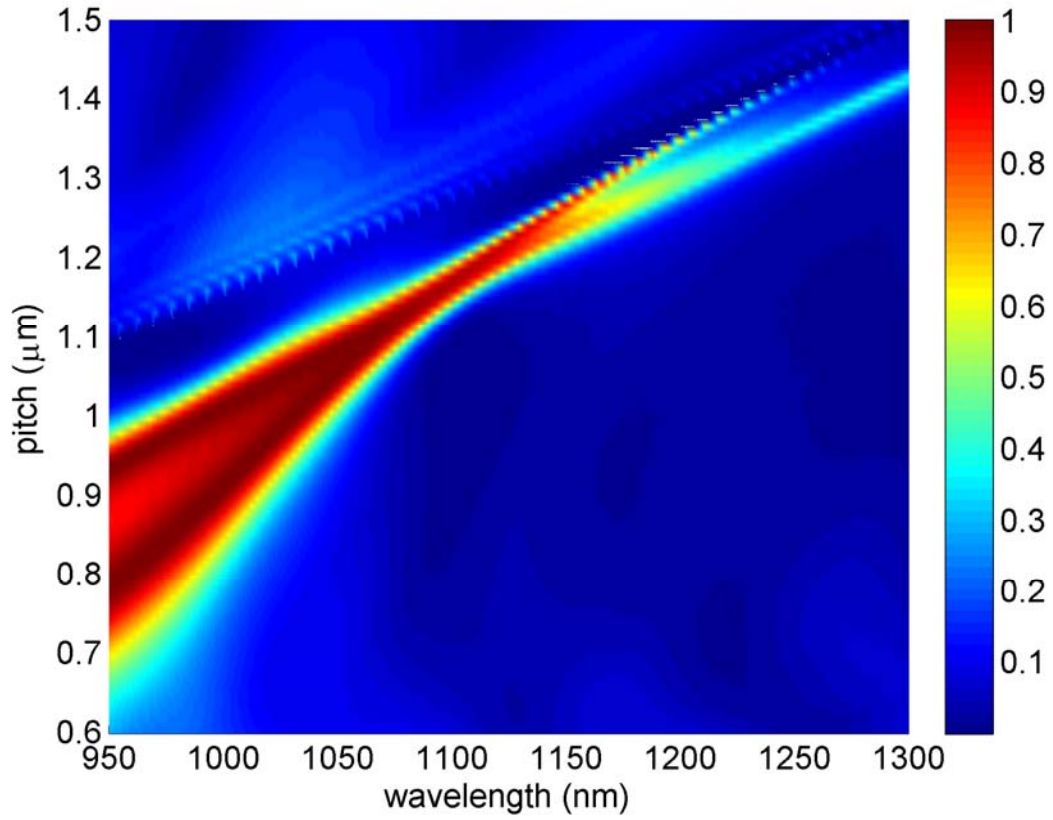
Fig. S1. Reflection spectrum with varying radius r$_{disc}$. Diamond mirror reflection spectrum at normal incidence for varying radius r$_{disc}$. Design parameters are: angle α = 70°, r$_{min}$ =50nm, r$_{support}$ =250nm, pitch 1.1μm, and height 3μm. Red and blue colors indicate locations of maximum and minimum reflection, respectively.
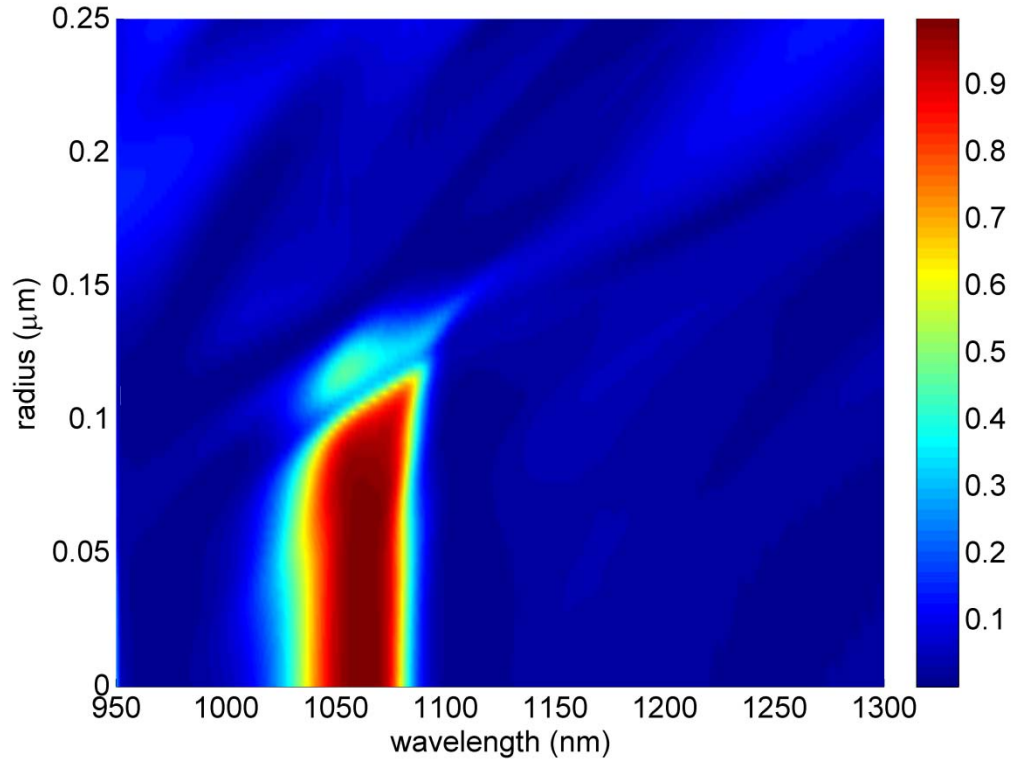
Fig. S2. Reflection spectrum with varying radius r_{min}. Diamond mirror reflection spectrum at normal incidence for varying radius r_{min}. Here, $\alpha = 70°$, $r_{disc} = 250$nm, $r_{support} = 250$nm, pitch 1.1μm, and height 3μm. Red and blue colors indicate positions of maximum and minimum reflection respectively.
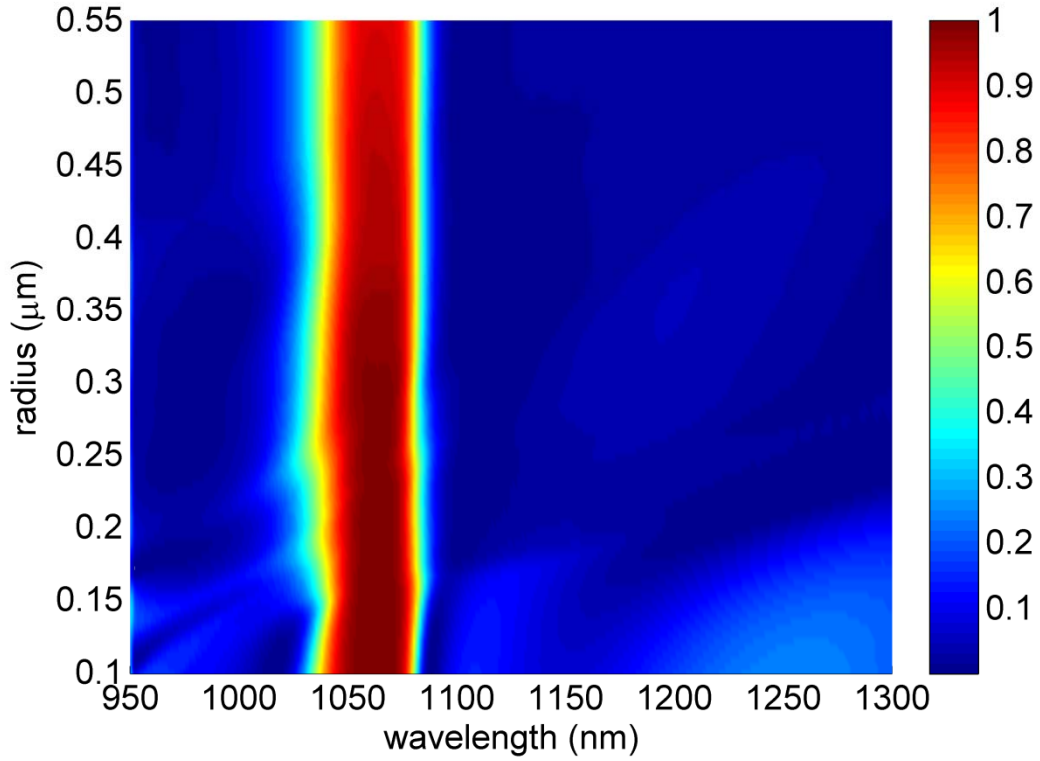
Fig. S3. Reflection spectrum with varying radius r_{support}. Diamond mirror reflection spectrum at normal incidence for varying radius $r_{support}$. Here, $\alpha = 70°$, $r_{disc} = 250$nm, $r_{min} = 50$nm, pitch 1.1μm, and height 3μm. Red and blue colors indicate positions of maximum and minimum reflection respectively.
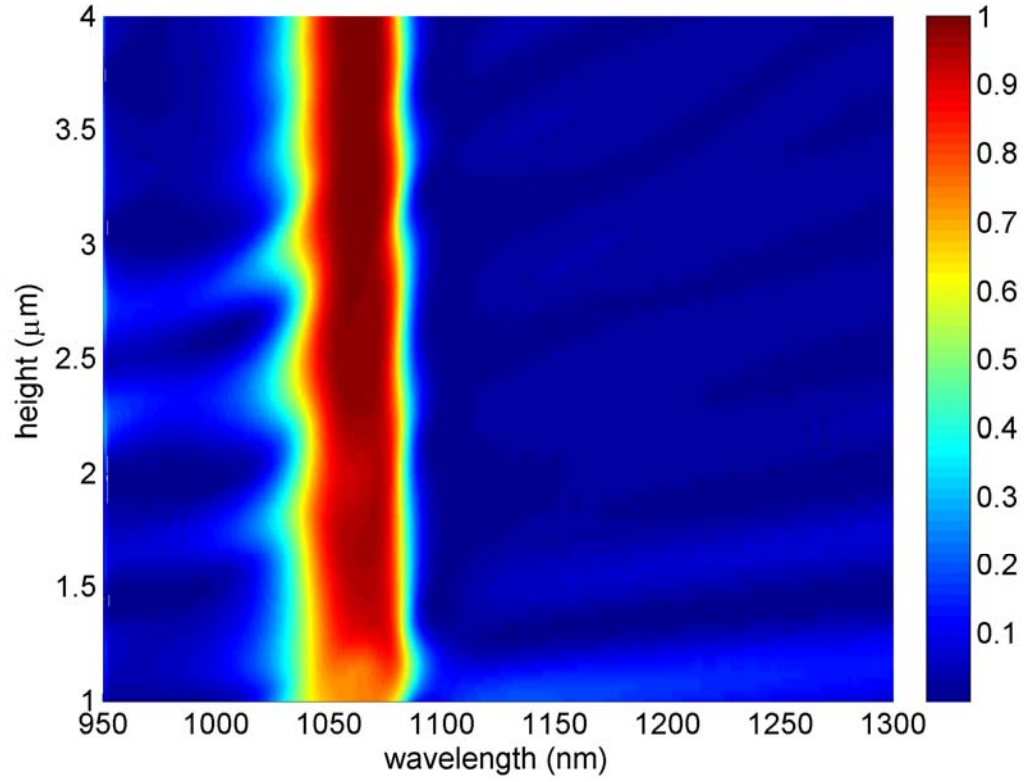
Fig. S4. Reflection spectrum with varying total device height _h_. Diamond mirror reflection spectrum at normal incidence for varying height _h_. Here, α =70°, , r_{disc} =250nm, r_{min} =50nm, radius $r_{support}$ =250nm and pitch 1.1μm. Red and blue colors indicate positions of maximum and minimum reflection respectively.

Fig. S5. Reflection spectrum with varying pitch. Diamond mirror reflection spectrum at normal incidence for varying pitch. Pitch is defined as the center to center distance of the golf tee columns in a hexagonal lattice. Here, α =70°, r_{disc} =250nm, r_{min} =50nm, $r_{support}$ =250nm and height 3μm. Red and blue colors indicate positions of maximum and minimum reflection respectively.
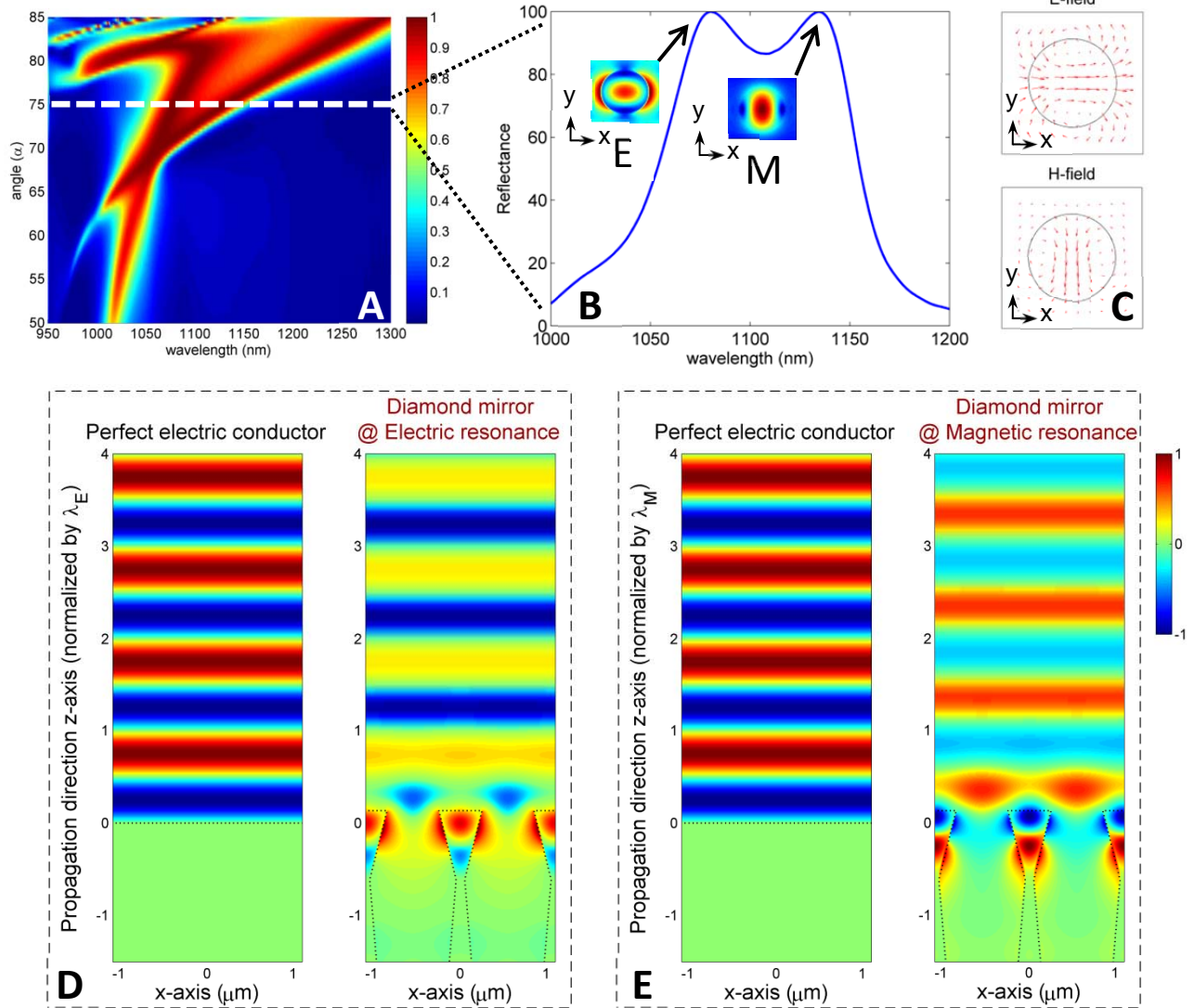
Fig. S6. Standing-wave patterns reflected from the diamond mirror and a perfect electric conductor (PEC) mirror. (A) Reflection spectrum of the diamond mirror, with a sectional line-cut at $\alpha = 75°$ indicated by the white dashed line. (B) Perfect reflection exists for both spectrally separated electric and magnetic modes. Insets show the electric and magnetic field plots in the x-y plane of the golf tee column. (C) Electric and magnetic field vector plots confirm the presence of electric and magnetic dipolar resonances in the golf tee column. E-field and H-field vectors are perpendicular to each other. (D) Standing-wave pattern of reflected light for the diamond mirror at the electric resonance compared to the reflection from PEC. 180° phase shift in the reflected light, characteristic for reflection from PEC, can be observed. The dotted black lines represent the PEC-air interface and the boundaries of the diamond nanostructures. The PEC surface is placed at a height equivalent to the center of the mode in the golf tee column. (E) In contrast, the diamond mirror excited at the magnetic resonance features a zero phase shift, as seen in standing wave pattern.
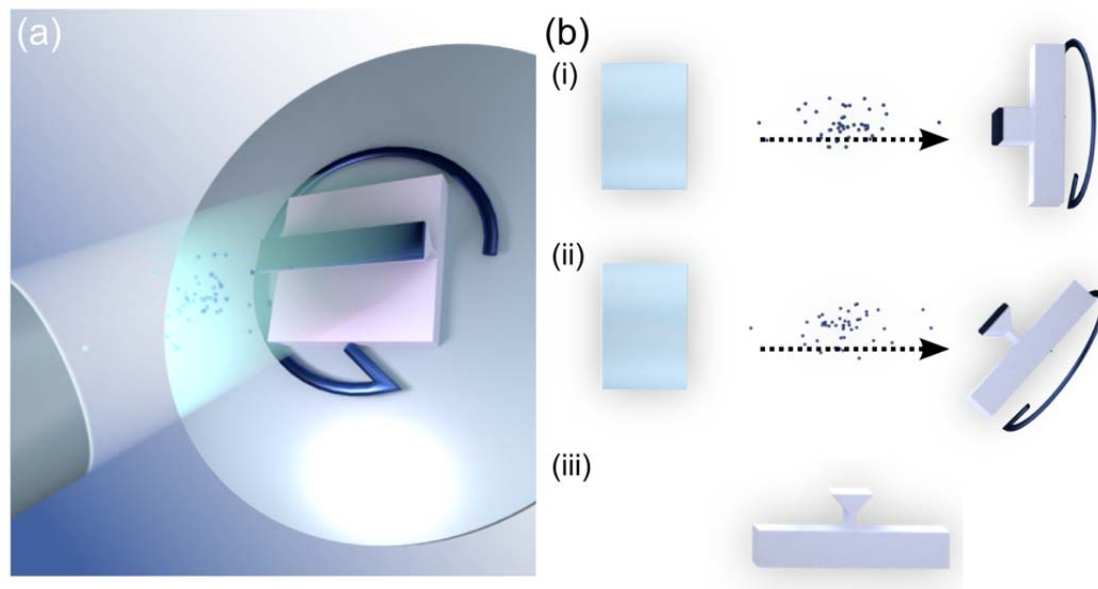
**Fig. S7. Reactive ion beam undercut etching (RIBAE).** (a) Graphical depiction of RIBAE. (b) RIBAE fabrication steps (i) Top-down etching of a sample mounted perpendicular to the ion beam path on a rotating sample stage. (ii) Sample tilted to obtain an acute angle between the sample and ion beam, uniformly etching underneath the etch mask. (iii) mask removal yielding undercut nanostructures from a bulk substrate.
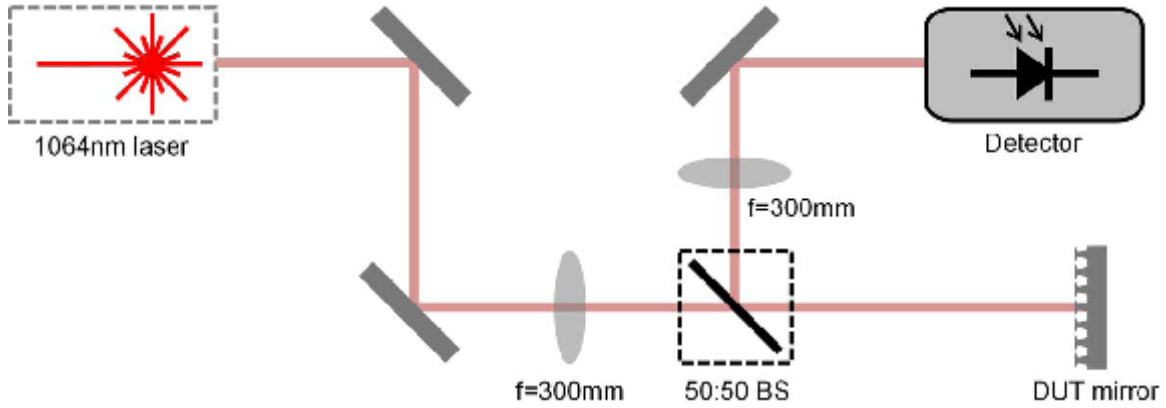
Fig. S8. Schematic of the experimental setup used for measuring the reflectance spectrum and absolute reflectivity. For spectral measurements a 1065nm superluminescence diode (InPhenix IPSDD1004C) is collimated and directed with broadband silver mirrors (Thorlabs PF10-03-P01). A 50:50 beamspiltter (Thorlabs CM1-BP145B3) is used to direct the reflected beam to an optical spectrum analyzer (Yokogawa AQ6370). Lenses are used to focus the beam to the sample (Thorlabs AC254-300-C-ML). For absolute reflectivity measurements the laser source is replaced by a 1064nm DBR laser (Thorlabs DBR1064S) and detected with a free space optical photodetector (Newport 918D-SL-OD3R).
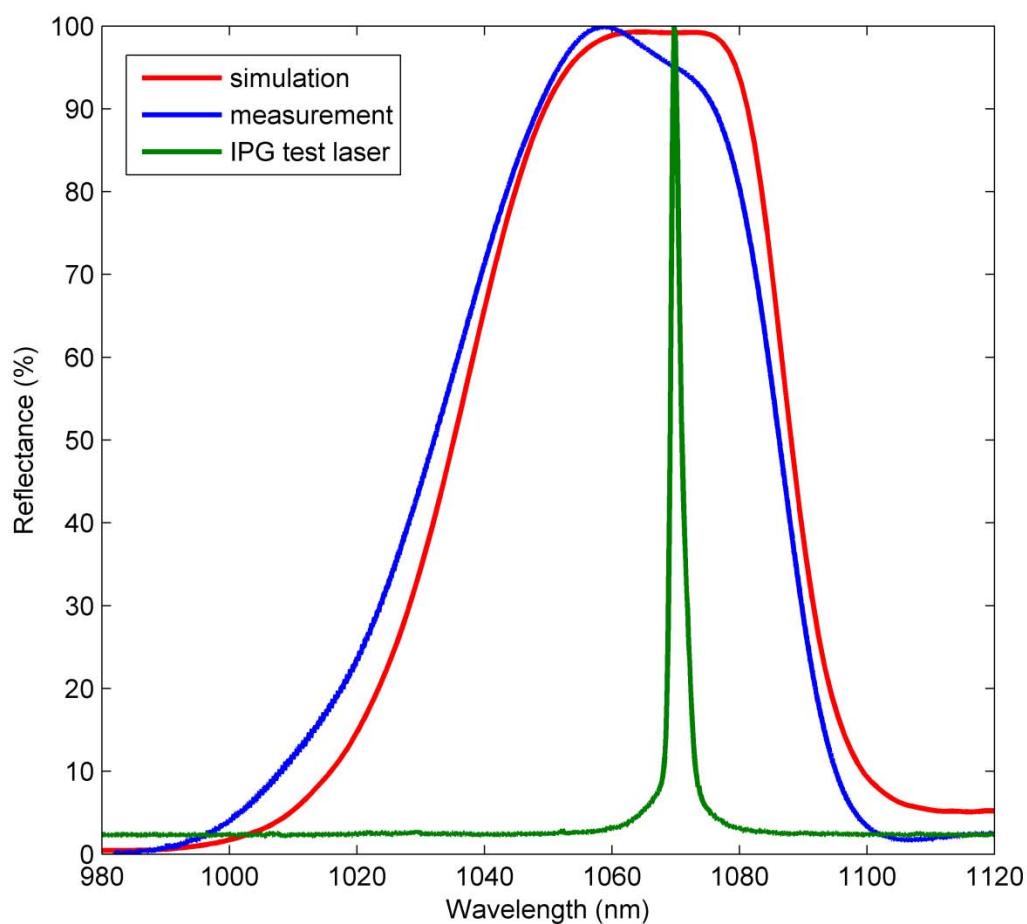
Fig. S9. Reflection spectrum of diamond mirror LIDT measurement at 1070nm. Diamond mirror measured (blue curve) and simulated (red curve) reflection spectrum at normal incidence. Green curve shows the spectrum of the 10kW IPG laser used during damage testing plotted in arbitrary units.
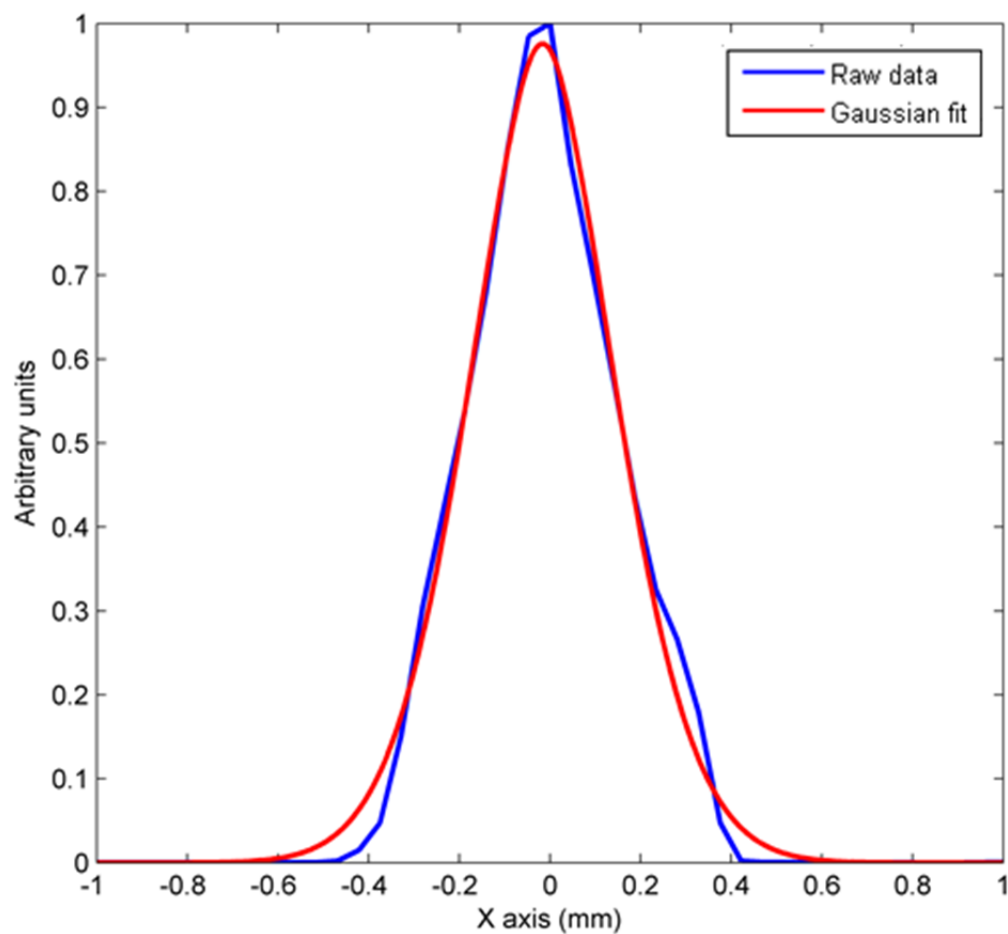
Fig. S10. Beam profile of 1070nm IPG LIDT test laser. Beam profile is collected using a Primes focus monitor. The focus monitor has a metal tip with a 20um pinhole in the side. The rotating tip then traverses the entire area of the beam, collecting 2D data of the beam profile. Blue line represents the raw data from the x-axis of the beam. The red line is the Gaussian fit.

Movie S1.

Thermal image video capture of LIDT test on diamond mirror at using a λ=1070 nm continuous wave (CW) laser, focused to a 750μm (1/e^2) diameter spot at 500W power, exposure for 60sec.

Movie S2.

Thermal image video capture of LIDT test on diamond mirror at using a λ=1070 nm continuous wave (CW) laser, focused to a 750μm (1/e^2) diameter spot at 2.5kW power, exposure for 60sec.

Movie S3.

Thermal image video capture of LIDT test on diamond mirror at using a λ=1070 nm continuous wave (CW) laser, focused to a 750μm (1/e^2) diameter spot at 5kW power, exposure for 60sec.

Movie S4.

Thermal image video capture of LIDT test on diamond mirror at using a λ=1070 nm continuous wave (CW) laser, focused to a 750μm (1/e^2) diameter spot at 7.5W power, exposure for 60sec.

Movie S5.

Thermal image video capture of LIDT test on diamond mirror at using a λ=1070 nm continuous wave (CW) laser, focused to a 750μm (1/e^2) diameter spot at 10kW power, exposure for 60sec.

Movie S6.

Video capture of LIDT test on diamond mirror at using a λ=1070 nm continuous wave (CW) laser, focused to a 750μm (1/e^2) diameter spot at 10kW power. Video helps illustrate the power leaking through the diamond and being absorbed by the water cooled mount which begins to glow.

References:

1. P. W. Baumeister, Optical coating technology. *Optimization* **10**, 7 (2004).
2. S. Fan, J. D. Joannopoulos, Analysis of guided resonances in photonic crystal slabs. *Physical Review B* **65**, 235112 (2002).
3. L. N. Taylor, A. K. Brown, A. J. Pung, E. G. Johnson, J. J. Talghader, Continuous-wave laser damage of uniform and nanolaminate hafnia and titania optical coatings. *Opt. Lett.* **38**, 4292-4295 (2013).
4. D. Ristau, *Laser-Induced Damage in Optical Materials*. (CRC Press, 2014).
5. D. Ristau, M. Jupé, K. Starke, Laser damage thresholds of optical coatings. *Thin Solid Films* **518**, 1607-1613 (2009).
6. G. Davies, *Properties and Growth of Diamond*. (Inspec, 1994).
7. M. Karlsson, F. Nikolajeff, Diamond micro-optics: microlenses and antireflection structured surfaces for the infrared spectral region. *Opt. Express* **11**, 502-507 (2003).
8. C. J. Brierley, C. M. Beck, G. R. Kennedy, J. Metcalfe, D. Wheatley, The potential of CVD diamond as a replacement to ZnSe in CO2 laser optics. *Diamond and Related Materials* **8**, 1759-1764 (1999).
9. A. M. Zaitsev, *Optical Properties of Diamond A Data Handbook*. (Springer, 2001).
10. W. Cai, V. Shalaev, *Optical Metamaterials: Fundamentals and Applications*. (Springer, 2009).
11. N. Engheta, R. W. Ziolkowski, *Metamaterials: Physics and Engineering Explorations*. (Wiley-IEEE 2006).
12. J. B. Pendry, D. Schurig, D. R. Smith, Controlling Electromagnetic Fields. *Science* **312**, 1780 (2006).
13. P. Qiao, W. Yang, C. J. Chang-Hasnain, Recent advances in high-contrast metastructures, metasurfaces, and photonic crystals. *Adv. Opt. Photon.* **10**, 180-245 (2018).
14. I. Staude *et al.*, Tailoring Directional Scattering through Magnetic and Electric Resonances in Subwavelength Silicon Nanodisks. *ACS Nano* **7**, 7824-7832 (2013).
15. N. Yu, F. Capasso, Flat optics with designer metasurfaces. *Nat Mater* **13**, 139-150 (2014).
16. N. Yu *et al.*, Light Propagation with Phase Discontinuities: Generalized Laws of Reflection and Refraction. *Science* **334**, 333 (2011).
17. F. Aieta, M. A. Kats, P. Genevet, F. Capasso, Multiwavelength achromatic metasurfaces by dispersive phase compensation. *Science* **347**, 1342 (2015).
18. M. Esfandyarpour, E. C. Garnett, Y. Cui, M. D. McGehee, M. L. Brongersma, Metamaterial mirrors in optoelectronic devices. *Nat Nano* **9**, 542-547 (2014).
19. A. V. Kildishev, A. Boltasseva, V. M. Shalaev, Planar Photonics with Metasurfaces. *Science* **339**, (2013).
20. Y. Yang, I. I. Kravchenko, D. P. Briggs, J. Valentine, All-dielectric metasurface analogue of electromagnetically induced transparency. *Nature Communications* **5**, 5753 (2014).
21. Y. H. Fu, A. I. Kuznetsov, A. E. Miroshnichenko, Y. F. Yu, B. Luk'yanchuk, Directional visible light scattering by silicon nanoparticles. *Nature Communications* **4**, 1527 (2013).
22. A. Arbabi, Y. Horie, M. Bagheri, A. Faraon, Dielectric metasurfaces for complete control of phase and polarization with subwavelength spatial resolution and high transmission. *Nature Nanotechnology* **10**, 937 (2015).

23.   M. Khorasaninejad, F. Capasso, Metalenses: Versatile multifunctional photonic components. *Science* **358**, eaam8100 (2017).
24.   M. Khorasaninejad *et al.*, Metalenses at visible wavelengths: Diffraction-limited focusing and subwavelength resolution imaging. *Science* **352**, 1190 (2016).
25.   S. Liu *et al.*, Optical magnetic mirrors without metals. *Optica* **1**, 250-256 (2014).
26.   P. Moitra, B. A. Slovick, Z. Gang Yu, S. Krishnamurthy, J. Valentine, Experimental demonstration of a broadband all-dielectric metamaterial perfect reflector. *Applied Physics Letters* **104**, 171102 (2014).
27.   P. Moitra *et al.*, Large-Scale All-Dielectric Metamaterial Perfect Reflectors. *ACS Photonics* **2**, 692-698 (2015).
28.   B. Slovick, Z. G. Yu, M. Berding, S. Krishnamurthy, Perfect dielectric-metamaterial reflector. *Physical Review B* **88**, 165116 (2013).
29.   J. D. Joannopoulos, S. G. Johnson, J. N. Winn, R. D. Meade, *Photonic Crystals: Molding the Flow of Light, 2nd ed.* (Princeton University Press, 2008).
30.   S. S. Wang, R. Magnusson, Theory and applications of guided-mode resonance filters. *Appl. Opt.* **32**, 2606-2613 (1993).
31.   Y. H. Ko, R. Magnusson, Wideband dielectric metamaterial reflectors: Mie scattering or leaky Bloch mode resonance? *Optica* **5**, 289-294 (2018).
32.   D. Rosenblatt, A. Sharon, A. A. Friesem, Resonant grating waveguide structures. *IEEE Journal of Quantum Electronics* **33**, 2038-2059 (1997).
33.   S. Tibuleac, R. Magnusson, Reflection and transmission guided-mode resonance filters. *J. Opt. Soc. Am. A* **14**, 1617-1626 (1997).
34.   H. L. Bertoni, L. h. S. Cheo, T. Tamir, Frequency-selective reflection and transmission by a periodic dielectric layer. *IEEE Transactions on Antennas and Propagation* **37**, 78-83 (1989).
35.   H. A. Atikian *et al.*, Freestanding nanostructures via reactive ion beam angled etching. *APL Photonics* **2**, 051301 (2017).
36.   H. A. Atikian *et al.*, Superconducting nanowire single photon detector on diamond. *Applied Physics Letters* **104**, 122602 (2014).
37.   E. Anoikin, A. Muhr, A. Bennett, D. Twitchen, H. de Wit. (2015), vol. 9346, pp. 93460T-93460T-93469.
38.   L. S. Meng, J. K. Brasseur, D. K. Neumann, Damage threshold and surface distortion measurement for high-reflectance, low-loss mirrors to 100+ MW/cm2 cw laser intensity. *Opt. Express* **13**, 10085-10091 (2005).
39.   C. S. Menoni *et al.*, in *Optical Interference Coatings 2016*. (Optical Society of America, Tucson, Arizona, 2016), pp. ThA.10.
40.   D. C. Brandt *et al.*, in *Emerging Lithographic Technologies XI*. (International Society for Optics and Photonics, 2007), vol. 6517, pp. 65170Q.